CVD growth of ultrapure diamond, generation of NV centers by ion implantation, and their spectroscopic characterization for quantum technological applications

T. Chakraborty,[1,*] F. Lehmann,[1] J. Zhang,[1] S. Borgsdorf,[2] N. Wöhrl,[3] R. Remfort,[3] V. Buck,[3] U. Köhler,[2] and D. Suter[1,†]

[1]*Fakultät Physik, Technische Universität Dortmund, D-44221 Dortmund, Germany*
[2]*Experimentalphysik IV, AG Oberflächen, Ruhr-Universität Bochum, D-44780-Bochum, Germany*
[3]*Faculty of Physics, University Duisburg-Essen and CENIDE, D-47057-Duisburg, Germany*

Applications of nitrogen-vacancy (NV) centers in diamond in quantum technology have attracted considerable attention in recent years. Deterministic generation of ensembles of NV centers can advance the research on quantum sensing, many-body quantum systems, multipartite entanglement, and so on. Here we report the complete process of controlled generation of NV centers in diamond as well as their characterization: growing diamond films through chemical vapor deposition (CVD), ion implantation, and spectroscopic characterization of the defect centers using a confocal microscope. A microwave-assisted CVD setup is presented which we constructed for the preparation of single-crystalline homoepitaxial diamond films. The films were prepared with minimized nitrogen concentration, which is confirmed through photoluminescence measurements. We demonstrate an *in situ* ultrahigh vacuum (UHV) implantation and heating process for creation of NV centers using a novel experimental setup. For the first time hot implantation has been shown which prevents surface charging effects. We do not observe graphitization due to UHV heating. By optimizing the implantation parameters it has been possible to implant NV centers in a precise way. We present large area mapping of the samples to determine the distribution of the centers and describe the characterization of the centers by spectroscopic techniques. Reducing the decoherence caused by environmental noise is of primary importance for many applications in quantum technology. We demonstrate improvement on coherence time T_2 of the NV spins by suppression of their interaction with the surrounding spin bath using robust dynamical decoupling sequences.

I. INTRODUCTION

Quantum technology exploits a handful of solid-state systems whose physical properties are determined by quantum effects. The nitrogen-vacancy (NV) color center, a defect center consisting of a substituted nitrogen atom and an adjacent vacancy embedded in a diamond crystal [1], is one of them. It has several attractive properties, including millisecond-scale spin coherence time, the possibility of manipulating the spins through microwave (MW) pulses, efficient optical initialization and detection of the spins, and the ability to perform such experiments at room temperature [2–4]. These properties make it a useful solid-state qubit system which has already been applied in a number of important quantum information experiments like demonstrating long quantum memory by controlling the spin qubits with high fidelity [5], coherently manipulating individual nuclear spins by specifically addressing a proximal electronic spin [6], exhibiting quantum entanglement between a photon and solid-state spin [7], demonstrating quantum interference between two photons [8,9], implementation of a quantum memory [10], and quantum repeater [11]. On the other hand, there has been a significant amount of progress in NV-based sensing technologies where

NV centers are applied in imaging the dynamics of neural network [12], living cells [13,14], probing of superconducting effects [15], sensing magnetic fields with high precision at the nanoscale [16–18], and others. Such promising applications have pioneered a way towards state-of-art NV-based quantum technology.

These sensing applications can be compared to other technological advancements like superconducting quantum interference devices [19], magnetic resonance force microscopy [20], Hall probe microscopy [21], and the optical atomic magnetometer [22] that have been introduced in past decades concerning sensing and imaging of magnetic field. Comparison shows that the novel method of magnetic field detection using the NV centers has several advantages over the more conventional techniques. For instance, the NV centers in diamond crystal can be prepared in a controlled fashion: The implantation process can be adjusted to reach a required density of NV centers at a depth of a few nanometers from the surface. This is an essential condition for efficient sensing as such shallow centers can be brought in close proximity (∼nm) to the magnetic centers under investigation. Importantly, diamond-based sensing can operate at room temperature, in liquid media and normal atmospheric conditions which gives more flexibility and feasibility to such applications. It has been experimentally demonstrated that diamond spins can detect weak magnetic field with high sensitivity and nanometer scale spatial resolution [14,16,17].

---

*tanmoy.chakraborty@tu-dortmund.de
†Dieter.Suter@tu-dortmund.de

The sensitivity of NV-based sensors is generally higher if ensembles of centers are used, rather than single centers. Sensing with dense ensembles of NV centers can increase the signal-to-noise ratio as the generated photoluminescence signal increases with N, the number of centers being used for detection. Thus, the magnetic sensitivity can be enhanced by a factor $1/\sqrt{N}$ when the field is homogeneous over the magnetometer area [17]. Furthermore, ensembles of centers are capable of imaging magnetic field over a wide field-of-view range [23].

Ensemble of centers has already been applied in different contexts like quantum metrology [12,24], quantum walk [25], device physics [26–28], and quantum simulations [29]. In this context, there have been a significant amount of efforts regarding growing highly pure diamond films and implanting clusters of NV centers with a target pattern suitable for the desired applications.

The primary motivation of this project is to generate ensembles of NV centers in ultrapure single crystal diamond films in a controlled way with the goal of optimizing them for applications in quantum information and sensing technology. The content of the paper has been mainly divided into three parts: The first part deals with growing highly pure single crystalline diamond films. The second part describes the precise creation of near-surface NV centers by ion implantation. In the third part we describe experimental methods for characterizing the centers and we also demonstrate experiments using various dynamical decoupling sequences with an aim to reducing the dephasing of the NV spins due to the environmental noise.

II. HOMOEPITAXIAL GROWTH OF DIAMOND

The microwave-activated plasma process [30] has been established as a more efficient technique for the deposition of high-quality single-crystal diamond films than other existing diamond growing techniques like high-pressure high-temperature (HPHT) crystal growth [31,32] or the hot-filament method [33]. In this work, pure single-crystal diamond films are homoepitaxially grown by chemical vapor deposition in a microwave-assisted CVD plasma source (CYRANNUS by iplas). We have developed and optimized an experimental setup for growing diamond films with minimum nitrogen concentration. A schematic diagram of our setup is shown in Fig. 1. The technology of the plasma source CYRANNUS is based on a cylindrical resonator with annular slots. The microwaves are fed into the ring resonator by a waveguide from which it is coupled into the cylindrical resonator of the reactor. Due to the centric position of the plasma in the reactor, the excitation without electrodes and the short mean free path at the deposition pressure of ca. 200 mbar the interaction of the reactive gas with chamber walls is minimized.

The homoepitaxial growth of diamond by CVD involves the deposition of carbon atoms on a diamond surface that originate from the dissociation of carbon-containing precursors in hydrogen gas. Hydrogen is essential because it selectively etches nondiamond carbon. For the deposition of pure diamond films the hydrogen in this work is generated in a hydrogen generator (HG-1200 by CMC Instruments GmbH)
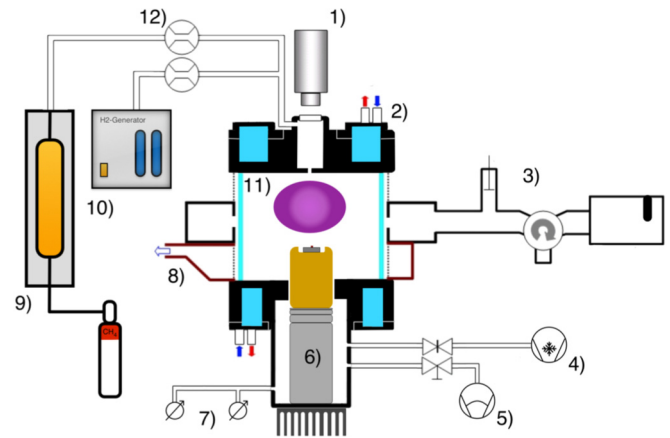

FIG. 1. Schematic representation of the experimental setup: (1) infrared pyrometer IS320 in line of sight with sample; (2) water cooling in top and bottom flange; (3) microwave feed consisting of magnetron, circulator, EH tuner, and ring resonator; (4) cryopump with plate valve; (5) backing pump; (6) multipart sample holder; (7) vacuum gauges; (8) air cooling; (9) methane gas purifier MonoTorr PS4-MT3-531; (10) hydrogen generator HG1200; (11) quartz cylinder; (12) mass flow controller.

with a purity of 99.99999%. The methane (5.0) is purified (SAES Pure Gas Inc.) to gas impurities <1 ppb. Diamond films are grown with a methane and hydrogen mixture with a typical ratio around 4%).

The chamber is evacuated with a scroll pump and a cryopump (CTI-Cryogenics 8200 compressor with cryo-torr pump) and reaches a base pressure of around 10^{-9} mbar. Mirror-polished single crystal Ib (001) diamonds (electronic grade) from Element Six Ltd. (<5 ppb nitrogen impurities) were used as substrates. Substrates were ultrasonically cleaned for 20 min in isopropanol and subsequently 20 min in acetone. During deposition the substrates were kept on a copper substrate holder. Prior to the deposition the substrates were etched in a H_2 plasma for 30 min at 170 mbar. After this cleaning step the process parameters were switched to the deposition parameters (Table I).

The thickness of the grown diamond films and comparison between purity of the substrate and films were determined by measuring PL depth profiles, as described in detail in Sec. IV B.

Raman spectroscopy was performed to determine the crystallinity of the synthesized diamond samples. The data (Fig. 2)

TABLE I. Relevant process parameters for the grown samples.

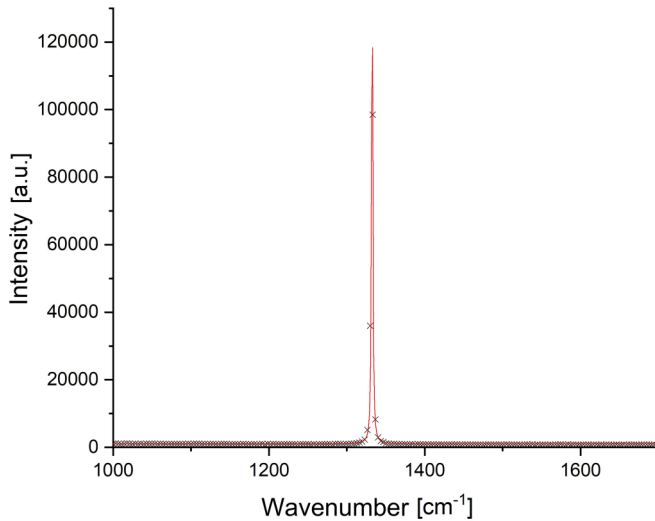| Parameters	Values
Pressure	170 mbar
Gas flow	400 sccm
H_2 fraction	96%
CH_4 fraction	4%
MW power	1.6 kW
Deposition time	8 h
Substrate	Diamond substrates Ib (001) (electronic grade)
Temperature	900 °C

FIG. 2. Raman spectroscopy of single crystal diamond.

show a sharp diamond peak at 1332.54 cm^{-1} with a full width at half maximum (FWHM) of 1.61 cm^{-1}. The narrow line proves the high crystallinity and even exceeds the values for natural and HPHT single crystals [34]. The position of the diamond peak indicates that there is almost no intrinsic stress in the grown films. Similar spectra were obtained over the whole surface area.

Secondary ion mass spectroscopy (SIMS) measurements were done to measure the impurities in the deposited diamond films. Since impurities were expected to come from the process gas, we measured the concentration of hydrogen, oxygen, and nitrogen in the films. For hydrogen and oxygen the signals were below the detection limits of the instrument. The upper limit of nitrogen concentration was determined using the approach of Gnaser *et al.* [35] as 1.3×10^{-7}(ca. 0.1 ppm). The only other element that was found in the diamond sample in relevant concentrations is silicon. It was measured in PL measurements with a strong ZPL at 738 nm originating from the silicon-vacancy center in diamond. The silicon is supposed to come from the plasma reactor walls since the vacuum chamber consists of a quartz recipient and the plasma has contact with the wall and etches silicon from the quartz. It was not possible to calculate the concentration of silicon from the PL measurements. Future SIMS measurements will include the determination of the concentration.

The incorporated nitrogen can only come from the process gases or the leakage of the vacuum system. By using a hydrogen generator (cmc Instruments GmbH, type HG1200-2T) and pure methane which was additionally purified (Mono Torr type PS4-MT3-531), the purity of the process gases used was 7.0 (99.99999%) for hydrogen and 9.0 (99.9999999%) for CH4, while the leakage of the vacuum chamber was estimated to be around 2.4×10^{-4} sccm. The nitrogen concentration of the grown layer is thus calculated to be below 1 ppb by assuming an incorporation rate of 10^{-4} [36].

III. ION IMPLANTATION

Two processes are currently used to generate NV centers in diamond. One process is to dose nitrogen in the process gas while growing the CVD diamond. In this process the NV centers are statistically distributed in a well-defined plane. It is possible to tune the thickness of this plane [37] and the density of NV centers. The second process is to implant nitrogen with an ion gun into the single crystal diamond [38]. For scalable quantum computer architecture and also for magnetometry applications, it is necessary to get control of the accurate positioning of the NV centers in all three axes together with a high probability of creation. It was shown that the yield of creating NV centers can be up to 50% with high implantation energies (2 MeV) [39] but the spatial resolution is very low. The depth and straggling depends on the ion energy and can be calculated with SRIM [24,40]. It is possible to increase the resolution by implanting with lower energies (1–5 keV) but in this case the yield of creation is reduced to 2.5% [41]. Also, the ion density has an influence on the yield [42], therefore it is important to get control of the beam current, the beam profile, and the implantation time. To create the NV centers it is necessary to anneal the diamond after the implantation up to 600°–800 °C for 2 h which is typically done under high vacuum conditions in a quartz oven after the diamond has been transferred from the implantation chamber. The annealing of the diamond under these conditions often leads to surface graphitization, which must be removed by etching in a boiling triacid [43].

The diamond surface before and after the implantation is still not well characterized, in particular the influence of the surface on shallow NV centers. To check how treatments influence the quality of the implantation, e.g. lead to a higher background in the confocal signal or harm the coherence time T_2 time we want to present a completely new all in ultrahigh vacuum (UHV) setup where the preparation of the diamond surface, the implantation, and the annealing process can be done *in situ* under UHV conditions. Additionally, only in an UHV environment completely nonterminated diamond surfaces can be prepared. As received diamonds from Element6 are typically terminated by oxygen because the sample was cleaned in boiling triacid after the CVD growth. If the diamond is not cleaned in this way, it is hydrogen terminated after the CVD growth. The influence of oxygen and hydrogen on the ratio NV$^-$/NV^0 has been investigated in detail [44] and it was also found that a hydrogen termination leads to a surface conductivity on diamond. Our setup gives us for the first time the chance to check systematically the influence of these typical surface terminations on the creation yield for NV centers by comparing them to a nonterminated surface. We use a conventional UHV chamber with a turbo molecular pump, an ion getter pump, and a titanium sublimation pump to achieve a base pressure of 5×10^{-11} mbar.

For low-energy nitrogen implantation we use a IQE 12/38 ion source from SPECS. The energy range of the ion gun goes from 400 eV up to 5 keV. The beam diameter (FWHM) is specified to be 150 μm. To get a very high purity of nitrogen a Wien-Mass filter is installed, which can also be used to switch between molecular or atomic nitrogen. As a source gas we use ^{15}N$_2$ with a purity of (98 atom %). ^{15}N nitrogen is used to ensure that the NV center was created by implanted nitrogen and not from an abundant one because even with a nitrogen concentration below 5 ppm there would be a chance of one native nitrogen atom in a volume of 150 nm^3. To measure

(a)

Ion gun
Z-Stage
Faraday cup
Aperture
Sampleholder
Manipulator
X-Y-Stage

(b)

• Cone
• Tantalum holder
• Diamond
• Wedge

(c)

• Tantalum holder
• Diamond
• Platinumfoil
• Thermo management diamond
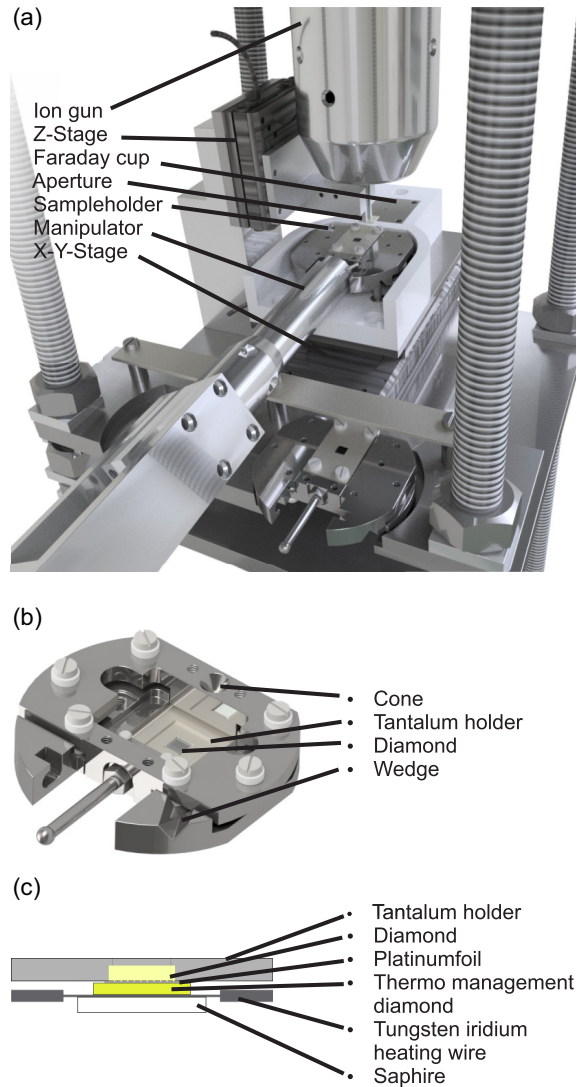• Tungsten iridium heating wire
• Saphire

FIG. 3. (a) Complete implantation stage. (b) Sample holder for precise placing. (c) Heating stack for effective heat transport.

the beam current a Faraday cup with shielding is installed. The beam diameter was calibrated and measured by scanning the beam over the edge of the Faraday cup. The last parameter which has to be controlled for a correct dose is the implantation time. An electric beam chopper allows one to switch on and off the ion beam in 1 μs and to do 15–1500 μs pulses. The sample position is controlled by an *XY*-nanopositioning stage from attoCube with a closed feedback loop. To control

the width of the implanted region, a tantalum aperture is used for first test experiments by melting a hole into the tantalum sheet with a diameter of $\sim$20 μm by a laser beam. The sputter yield for nitrogen on tantalum with 5 keV is very low. So it can be assumed that the contamination of diamond by tantalum is negligible. The aperture is connected to ground to prevent any charging effect and the focus point of the ion beam is set below the sample to achieve a more parallel beam path. The position of the aperture with respect to the sample surface is controlled by a *Z*-nanopositioning stage. The sample holder [see Fig. 3(b)] was designed to transfer the diamond into the UHV chamber and to the implantation stage below the ion gun [see Fig. 3(a)]. The accuracy of placing the sample is below 5 μm, which was achieved by a cone and wedge placement design. Also it is important to heat the diamond in UHV up to 900 °C while maintaining a pressure of 1×10^{-10} mbar. To achieve this we have designed an effective heating stack [see Fig. 3(c)].

The thermo-management diamond has a very good thermal conductivity of 2000 W/Km at room temperature. Also at 900 °C its conductivity is significantly higher than that of sapphire. The platinum foil also collects the thermal radiation of the tungsten iridium heating meander and does not react with the diamond. With this setup we need 12-W electric power to reach 900 °C on the diamond. Additionally a four-point Van-der-Pauw measuring station was installed in the UHV system to determine the surface conductivity of the diamond after different surface treatments of a pure heated diamond in UHV.

Mapping of the diamond samples was performed with a setup without the *XY* stage and the aperture as it is shown in Fig. 3. To check the influence of different surface treatments on the localization and shape of the implanted area, five implantations were made under different conditions which are discussed below. Table II provides an overview of the main sample preparation parameters. Starting from a base pressure of 5×10^{-11} mbar the diffuse N_2 pressure during implantation rose to 2×10^{-8} mbar. The dose was 1×10^{12} cm^2 and the beam was focused at the center of the sample. They were heated at 800 °C for 2 h under a vacuum of 2×10^{-10} mbar after the implantation. Sample 1 (S1) was hydrogen terminated and the implantation was done at room temperature. To check the surface conductivity we use the Van-der-Pauw setup (see inset of Fig. 4). The hydrogen-terminated diamond shows a conductance of 1×10^{-3} S/m at atmospheric conditions and it drops to 3×10^{-4} S/m in UHV which was also reported in [45]. Sample 2 (S2) was cleaned before the implantation by heating the sample up to 800 °C for 12 h under a vacuum of

TABLE II. The table shows the main information for the samples S1–S5. The postheating for all the samples was done at 800°C for 2 h. All experiments were done under UHV conditions.

| Sample	Precleaning	Termination	Aperture	Dose (cm^2)	Implantation temperature (°C)
S1	Isopropanol, acetone	Hydrogen	No	1×10^{12}	Room temperature
S2	Isopropanol, acetone heated at 800 °C	Bare	No	1×10^{12}	Room temperature
S3	Isopropanol, acetone, heated at 800 °C	Bare	No	1×10^{12}	700
S4	Isopropanol, acetone, heated at 800 °C	Bare	No	1×10^{17}	700
S5	Isopropanol, acetone, heated at 800 °C	Bare	Yes	4×10^{15}	700
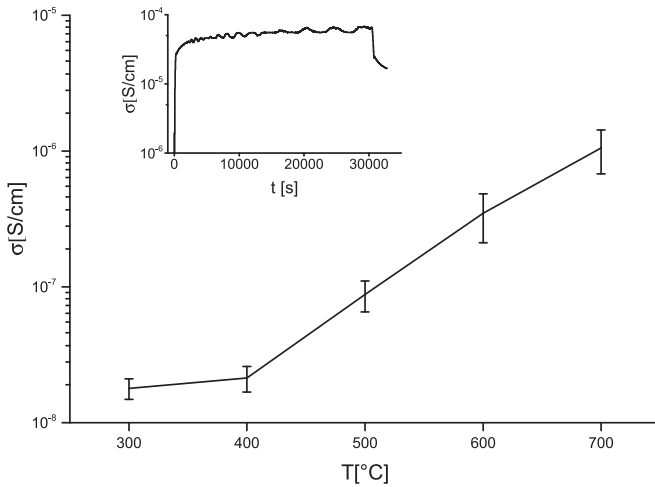
FIG. 4. Van-der-Pauw conductance measurement in UHV. (Inset) Time-dependent measurement of a hydrogen-terminated diamond at room temperature. The initial fast increase of the conductivity occurs after exposing the hydrogen-terminated diamond without any adsorbates from vacuum to atmospheric conditions. After 30 000 s the diamond was placed again in a vacuum environment, which leads to a drop of the conductivity. (Bottom) Temperature-dependent conductivity of nonterminated diamond.

2×10^{-10} mbar. After this treatment the sample was no longer hydrogen or oxygen terminated [46,47]. Sample 3 (S3) was in the same way cleaned as S2 but the implantation was done at $700\,°C$. To check if the heating treatment leads to a higher surface conductivity we measured the surface conductivity for different temperatures of a nonterminated diamond with the Van-der-Pauw setup (Fig. 4). It can be seen that the conductance raises up to 1×10^{-6} S/m at $700\,°C$, which is more than two orders magnitude lower than for S1 but it seems that the electrical conductivity is sufficient to prevent charging during the ion implantation. Optical characterization of the implanted NV centers in S1, S2, and S3 are discussed in Sec. IV (C). In Sec. IV B we have demonstrated large area confocal mapping of samples S4 and S5 whose preparation procedures are described below: In the case of S4, the sample was cleaned with isopropanol and acetone, heated in UHV (5×10^{-10} mbar) at $700\,°C$ for 2 h, ion implantation without an aperture was performed with an ion dose of $1 \times 10^{17}\,cm^{-2}$, and finally heated at $800\,°C$ for 2 h. For sample S5, we implanted four dots in a row with a dose of $1 \times 10^{15}\,cm^{-2}$ and two dots with a dose of $1 \times 10^{12}\,cm^{-2}$ with the same conditions as for S3.

IV. OPTICAL CHARACTERIZATION

For a quantitative characterization of the samples and to check the success of the implantation, we combine confocal scanning microscopy with optical spectroscopy. To allow scanning of complete samples, with length scales of a few mm with high resolution, we combined a piezoelectrical nanopositioning system (NP) with a motorized micropositioning stage (MP).

A. Setup

Figure 5 shows a schematic representation of the corresponding setup. A diode-pumped solid-state CW laser, which emits at 532 nm, is used for excitation. An acousto-optical modulator (extinction ratio 57 dB) is used to switch the laser beam on and off. The laser beam subsequently passes through an oil immersion microscope objective (MO) of numerical aperture 1.4, which focuses it into the diamond sample. The PL signal, propagating in the opposite direction of the laser beam, is collected by the same MO and separated from the scattered laser light by the dichroic mirror. The transmitted PL signal is collected into an optical fiber, passes through a 550-nm-long pass filter and is measured by a photon-counting detector. Alternatively, it can be sent through a monochromator for spectral analysis. The spot size diameter of our confocal setup was $0.46\,\mu m$. The optical fibers in the detection part provide the flexibility to switch between different types of measurements. The signal from a MW signal generator (APSIN) and an arbitrary waveform generator (AWG) are combined to generate the MW signal for exciting the electron spin transitions of the NV centers. A switch generates MW pulses, which are passed through a 16-W amplifier and a Cu wire attached to the diamond sample.

The confocal microscope combines a nanopositioning (NP) stage with a maximum traveling range of $70\,\mu m \times 70\,\mu m$ in the XY plane and $50\,\mu m$ along the Z direction with a motorized micropositioning (MP) stage, as shown in the bottom right of Fig. 5. The MO is attached to the NP stage whereas the sample is attached to the MP stage. With this setup, we can scan areas of up to 25×25 mm and generate PL images of XY planes at different depths covering the full diamond samples with nanometer resolution.

B. Confocal scanning microscopy

Figures 6(a) and 6(b) shows the measured full scans of the surfaces for samples S4 and S5, respectively. The important parameters used for preparing S4 and S5 can be found in Table II. The three regions marked by ovals in S5 were irradiated with the focused ion beam to generate NV centers; they clearly show the largest fluorescence rates. The parameters for implantation are given in Sec. III. Figure 6(c) shows that the spot size ($\Delta x = 15\,\mu m$, $\Delta y = 27\,\mu m$) is quite similar to the aperture size of the ion gun. In order to standardize the preparation conditions, instead of preparing the ensembles of centers throughout a diamond substrate, with different implantation parameters like temperature, heating time, ion dose, etc., we implanted several NV spots on a single sample and characterized them. This saved both the time and the cost of the diamond substrates. Through these implantations, we also gained better control on precisely creating spots with NVs. Such control is necessary for many quantum technological applications. For example, in case of electrical spin read-out, the NVs should be precisely created in certain positions between the electrodes [48]. Figure 6(c) shows an enlarged view of one of the four implanted spots marked by the oval as shown by the arrow. From the mapping image shown in Fig. 6(c), we can conclude that the size and position of the implanted area can be controlled in a deterministic way. The PL mapping also indicates that the deposited diamond layer
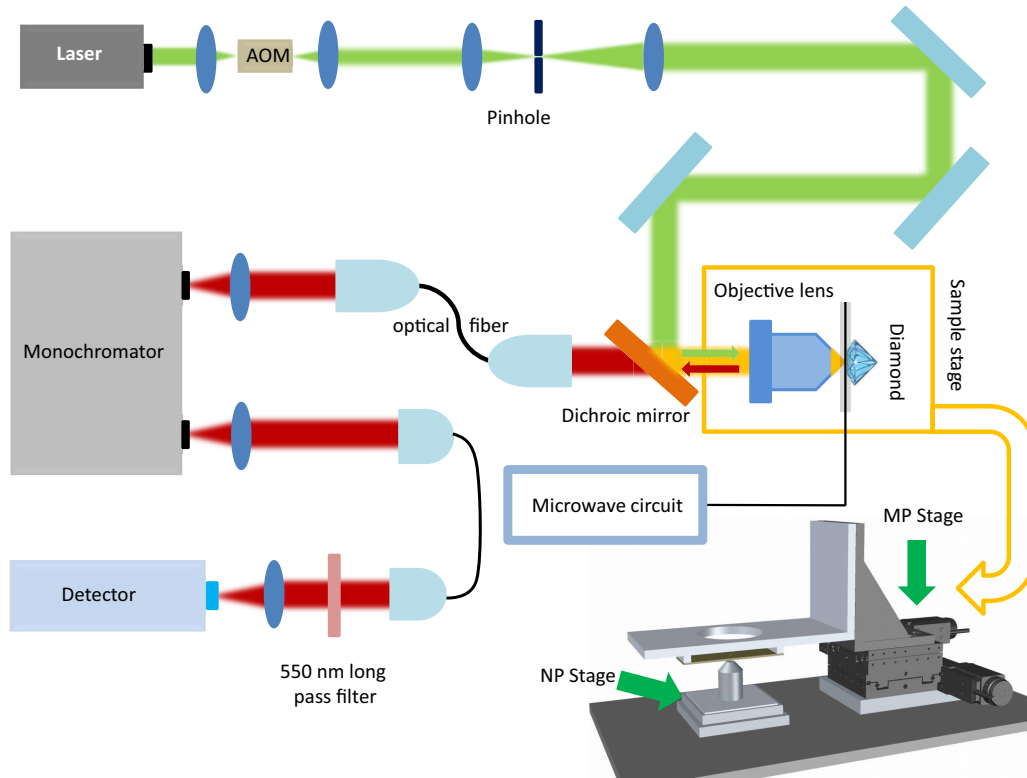
FIG. 5. Schematic diagram of the homebuilt confocal microscope. It includes a monochromator and a microwave circuit for exciting the electron spin transitions of the NV centers. The bottom right part of the figure shows a 3D representation of the positioning system, which combines a nanopositioning (NP) stage with a micropositioning (MP) stage to allow large area scans with high resolution.

appears to be quite clean. The spectroscopic characterization of this fluorescent spot is described in Sec. IV C.
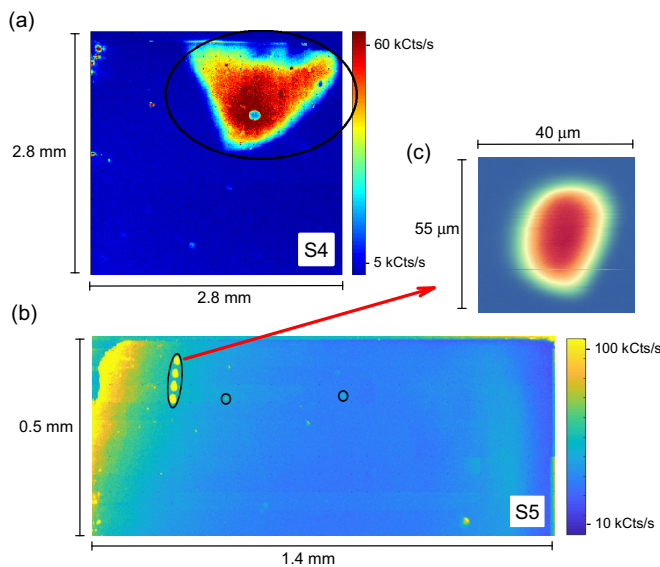

FIG. 6. (a) and (b) The full area confocal scan images for samples S4 and S5 (details mentioned in Sec. III, specifically in Table II). The ovals mark the regions where ions were implanted to generate NV centers. The color bars on the right-hand side of the images indicate the corresponding count rates. (c) An enlarged view of one of the implanted spots as shown by the arrow.

The blue area of the sample S4 corresponds to count rates of $\approx 5000\,\mathrm{s}^{-1}$, which is close to the background rate of our system. In this region, the diamond is very clean, with a very low defect density.

We used similar measurements to characterize the sample along the direction perpendicular to the surface. Since the thickness of the grown films is a few hundred micrometers, we again combined the MP and NP stages to provide sufficient traveling range. We performed spatially resolved PL measurements where the focal position of the MO was varied along the Z direction through the film. Figure 7 shows a depth-profile measured at the position indicated in the inset. The data indicates that the film thickness is around $265\,\mu$m. The recorded count rate in the grown layer is close to the background rate and is less than the count rate in the substrate, which indicates that the CVD-grown film has significantly higher purity than the substrate. The relatively thick diamond films of 265 μm were grown to have high-purity "bulklike" diamond films for the implantation of nitrogen. We wanted to ensure that the impurities in the diamond substrate do not affect the investigations of the NV centers on the grown layer. However, the deposition process is very customizable and films can be grown as thin as a few nanometers as well as up to millimeter thickness. On the other hand, the distance of the NV centers from the surface is determined by the energy of the nitrogen ions. The energy range of the ion gun goes from 400 eV up to 5 keV resulting in a depth of the NV centers between sub-nanometer scale and 10 nm below the surface of the grown layer. For our samples the depth was between 7 and 10 nm.
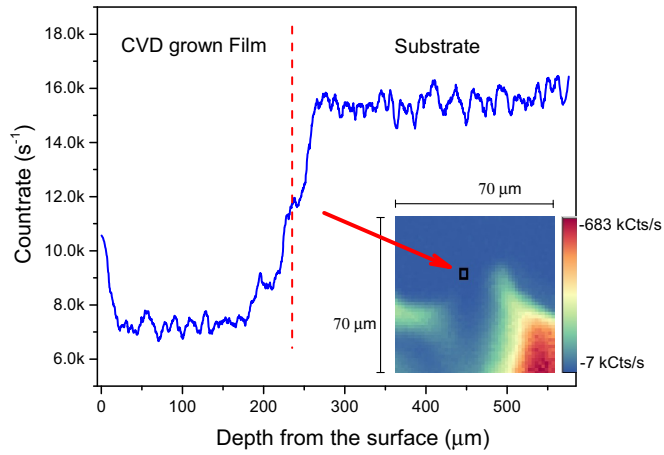
FIG. 7. Depth profile for CVD-grown diamond film on an electronic grade substrate from Element Six. The vertical line marks the boundary between the CVD-grown film and the substrate. The inset indicates the scanned image of the position where the depth scan was performed.

FIG. 9. Four spectra taken at different positions near the implantation spot for sample S5. The positions range from an area of strong signal near the center to the edge, where the count rate is low. The inset shows the spatial distribution of the PL intensity.

C. Optical spectroscopy

The successful formation of NV centers in the grown diamond films was confirmed by measuring spectra of the the fluorescence emitted by these regions. For each experiment a $2 \times 2 \, \mathrm{mm}^2$ map with $50 \times 50 \, \mathrm{pixel}^2$ was done with a Renishaw Raman spectrometer as a simple spatially resolved spectrometer. At each pixel we recorded a PL spectrum. Figure 8(d) shows some of these spectra. The peaks in the spectra are associated with NV^0 ZPL at 575 nm (curves 1 and 3) or NV^- ZPL at 637 nm (2). An overview of the position and shape of the implanted areas was obtained using the mapping method described above. The details about the samples are mentioned in Table II. The map of sample S1 in Fig. 8(a) shows a spot at the center of the diamond with a diameter of $\sim 200 \, \mu m$ and a halo of $\sim 400 \, \mu m$, which is the spot size that we expected from our experimental condition

for implantation: The ion gun was operated with an emission current $\sim 100 \, \mu A$. Using smaller apertures, we obtained smaller spots, such as the one shown in Fig. 6(c), which has a diameter of $\sim 25 \, \mu m$, obtained with an ion beam current of 500 pA. The spectrum for S1 shows the zero phonon lines (ZPL) of NV^0 at 575 nm and of NV^- at 637 nm, the second-order Raman peak between 600 and 620 nm, and a peak at 589 nm that is associated with some point defects possibly created during ion implantation [49]. In Fig. 8(b) S2 shows a strong enlargement of the implantation region on the diamond surface to the lower left corner of the sample. As described in Sec. III, this implantation was performed with a nonterminated and therefore electrically insulating diamond surface. Accordingly, the charges deposited by the beam result in surface charging and subsequent defocusing of the beam. This shows that the bare diamond surface at room temperature is not suited for localized nitrogen implantation at the low energies required for shallow NV centers. The peak for NV^- has a lower count rate than in the sample S1, which indicates a lower density in the laser stimulated area, caused by the broadening of the beam. The spectrum for S3 shown in Fig. 8(c) is similar to that of S1 but has slightly stronger features. S3 shows a sharp spot of $\sim 150 \, \mu m$ diameter without a bright halo. Using the relative ZPL intensities of NV^0 and NV^- charge states for S1, S2, and S3, we estimated their approximate concentration ratios $C_{NV^0} : C_{NV^-}$ of the measured spots following the method described in Ref. [24]. We obtained that $C_{NV^0} : C_{NV^-}$ equals 0.71, 2.8, and 1.5 for S1, S2, and S3, respectively.

Figure 9 exhibits a set of four spectra measured using the monochromator integrated with the confocal setup (as described in Sec. IV A) at different positions ranging form close to the center of the implanted area towards the periphery, as shown in the inset. The data clearly show the zero phonon lines (ZPL) at 575 nm and 637 nm associated with the NV^0 and NV^- centers, respectively, and the corresponding phonon side bands.
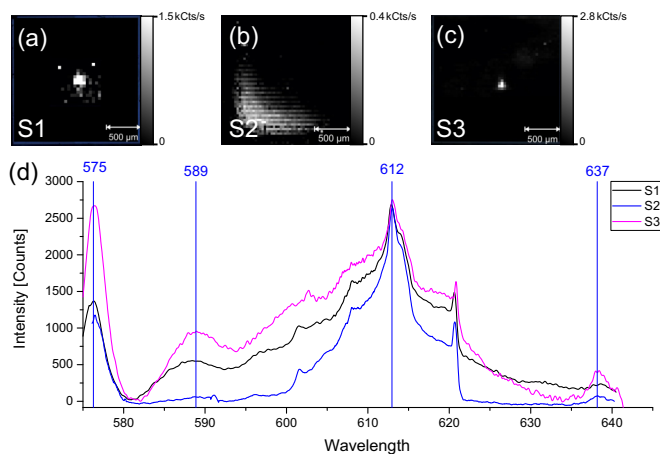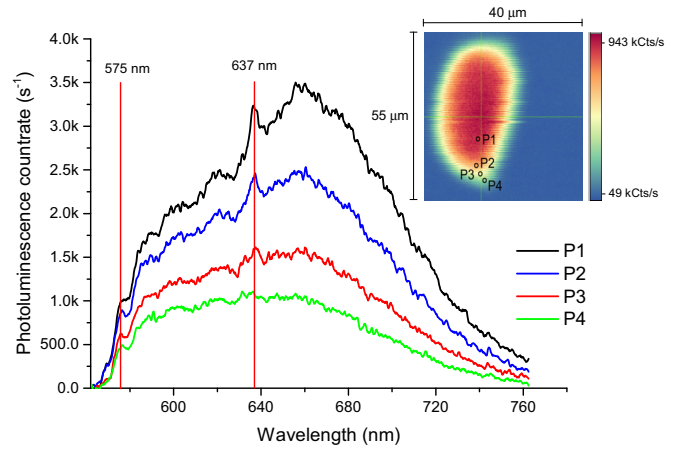

FIG. 8. Overview maps $(2 \times 2 \, \mathrm{mm}^2)$ of the diamond samples S1 (a), S2 (b), and S3 (c). The contrast is given by the counts of the NV^0 ZPL at 575 nm (a) and (c), or NV^- ZPL at 637 nm (b). The spectra at the bottom are taken from the pixels with the highest intensity.
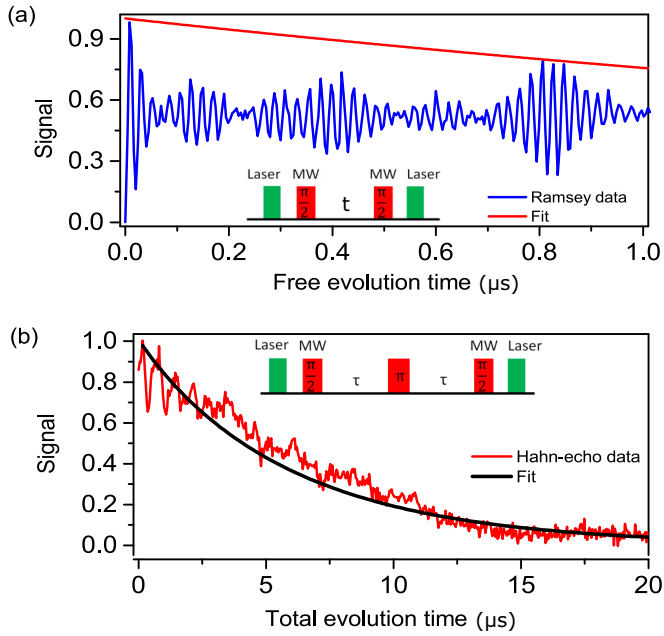
FIG. 10. (a) Free induction decay of the NV spins and (b) decay of the coherence of an ensemble of NV spins measured using the Hahn-echo sequence. The corresponding pulse sequences are shown as insets.

V. SPIN PROPERTIES

In this section we describe measurements of the coherence properties of the NV centers by electron spin-dependent fluorescence measurements at room temperature. The negatively charged NV center forms a triplet ground state where the zero field splitting separates the $m_S = 0$ and ± 1 states by ~ 2.87 GHz [50,51]. An external magnetic field lifts the degeneracy of the $m_S = \pm 1$ levels and of the ODMR lines. As an ensemble of NV centers consists of four possible symmetry axes, an applied magnetic field along an arbitrary direction projects itself onto the four axes with four different field values which creates four pairs of electronic transitions and hence eight lines in the ODMR data [52]. In our experiments, the orientation of the applied field was along such a direction that the components of the applied magnetic field along the four possible NV axes of the ensemble we measured had similar values, resulting in only two lines in the ODMR spectrum. The magnitude of the applied magnetic field was 16 Gauss. By scaling the photoluminescence with respect to the signal from a single center we estimated the concentration $\aleph$ of the NV centers in the spot in which we performed the ODMR measurements as $\aleph = 22$ ppm. To measure the coherence properties, we used different experiments that first initialized the system into the bright state ($m_S = 0$) by a 5-μs laser pulse. From this state, the coherence is generated and manipulated by resonant microwave pulses and the final state is read out by counting fluorescence photons during a second laser pulse whose optimal duration is ~ 400 ns [51].

Figure 10(a) shows the resulting free-induction decay (FID) signal, measured with a Ramsey-type [53] experiment where two $\frac{\pi}{2}$ pulses separated by a free evolution period t were applied between the initialization and read-out laser

pulses. The first $\frac{\pi}{2}$ pulse, with a frequency of 2.8272 GHz, generates a superposition of the spin states $m_S = 0$ and -1, which subsequently evolves for a time t. The second $\frac{\pi}{2}$ pulse converts one component of the coherence back into the population which is measured during the read-out step. The observed oscillation frequency of 50 MHz is the difference between the carrier frequency of the microwave between the two pulses and the transition frequency. The beats are due to the hyperfine coupling between the electron spin and the ^{14}N nuclear spin. We fitted the envelope of the FID signal to the expression e^{-t/T_2^*}, and calculated $T_2^* = 3.6$ μs.

To measure the coherence time T_2, we used the spin-echo sequence introduced by Hahn [54]. The sequence starts with the 5-μs initialization laser pulse followed by three MW pulses separated by free precession periods τ: $\frac{\pi}{2} - \tau - \pi - \tau - \frac{\pi}{2}$. The first $\frac{\pi}{2}$ pulse creates a coherent superposition of the $m_S = 0$ and -1 states and the last one converts the coherence into population difference. The π pulse inverts the accumulated phase, resulting in zero overall phase after the second free precession period, provided the environment is static. The experimental data in Fig. 10(b) show the decay of the coherence of the ensemble of NV spins. The envelope of the decay curve is fitted to the expression $e^{-(t/T_2)^p}$, where $t = 2\tau$ and the exponent p depends on the magnetic environment [55,56]. We obtained T_2(Hahn echo) $= 6.4 \mu s$ and $p = 0.96$.

Preserving the coherence of quantum states on a longer timescale is essential for quantum information and sensing protocols [5,28,57]. Decoherence of the spins belonging to NV centers happens due to their undesired interaction with the magnetic environment mainly caused by the electronic spins of substitutional nitrogen centers and ^{13}C nuclear spins [58–61]. To protect quantum states from decoherence, dynamical decoupling (DD) has been established as an efficient technique [62,63]. It decouples the system spins from the surrounding spin bath by applying a periodic sequence of inversion pulses that effectively isolate the system spin from the environmental noise [55,56,58,60,64].

Here, we demonstrate that the electronic spins in our samples respond well to the dynamical decoupling sequences and we are able to extend the coherence time T_2 beyond the values obtained in the Hahn-echo measurements described above. For this purpose, we use the Carr-Purcell-Meiboom-Gill (CPMG) pulse sequence, a robust DD technique which has been extensively used in NMR spectroscopy [62]. The CPMG sequence can be considered as an extended version of the Hahn-echo sequence where multiple refocusing π pulses are applied during the free evolution period between the two $\frac{\pi}{2}$ pulses, as shown in Fig. 11(a). We implemented CPMG sequences with the number n of control pulses varying from 4 to 64. The measured decoherence curves as a function of total free evolution time $t = 2n\tau$ and their fit to the expression $e^{-(t/T_2)^p}$ are plotted in Fig. 11(b). We have determined the coherence time $T_2(n)$ for the ensemble of NV spins from the above analysis and observed its extension by almost 29 times for 64 pulses [$T_2(64) = 173$ μs] over the corresponding value measured by the Hahn echo. The variation of T_2 with n is shown in Fig. 11(c). We also measured the spin-lattice relaxation time for the same ensemble of NV centers. Figure 11(d) shows the measured data along with the theoretical fit to the
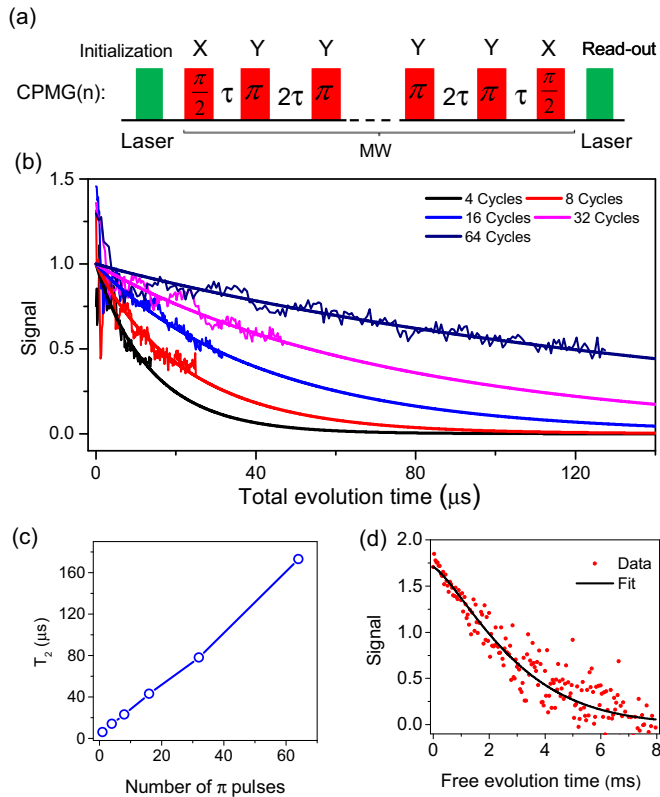
FIG. 11. (a) CPMG control sequence for variable number of refocusing π pulses. (b) Measured coherence decay data for an ensemble of NV spins for 4, 8, 16, 32, and 64 number of π pulses. The signal is in arbitrary units. The thick solid lines represent the fitted curves. (c) Variation of T_2 with the number n of CPMG π pulses. (d) T_1 relaxation for the electronic spin.
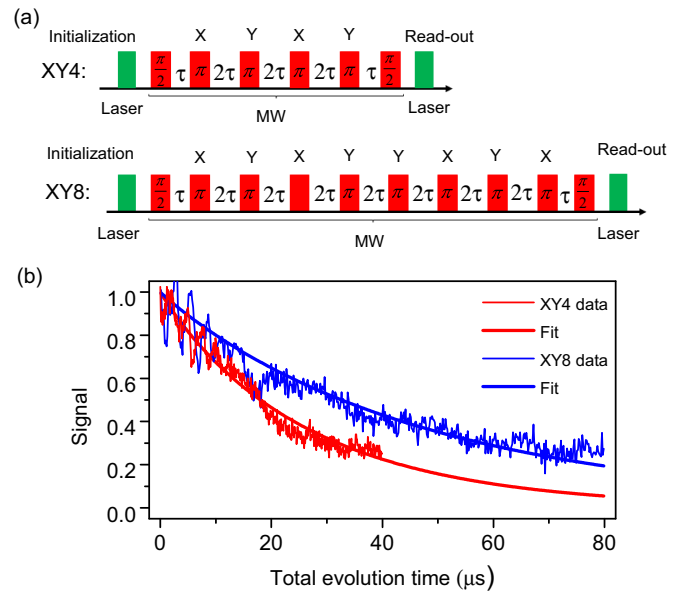

FIG. 12. (a) XY4 and XY8 dynamical decoupling sequences. (b) Coherence decay curves for multiple NV spins measured using XY4 and XY8 control sequences along with their theoretical fits to the expression $e^{-(t/T_2)^p}$ where t equals 8τ and 16τ for the XY4 and XY8 sequences, respectively.

expression $e^{-(t/T_1)^q}$. We obtained $T_1 = 3.14$ ms and $q = 1.32$. For short echo times, a part of the signal decays more rapidly. This appears to be due to some initial transients that precess around the effective field but die out after a few microseconds.

While the CPMG sequence is well suited for preserving a given quantum state, it is rather unsuited for protecting unknown quantum states [65,66]. For such cases, it is therefore important to use a pulse sequence that performs well for arbitrary initial conditions. We therefore repeated the measurement with the pulse sequences XY4 and XY8. They are well established as robust and symmetrized sequences [59,61,65,66]. They consist of a series of π pulses around two perpendicular rotation axes as shown in Fig. 12(a). The experimental decay curves obtained with the XY4 and XY8 sequences are shown in Fig. 12(b) together with the corresponding fits. We were able to extend T_2 up to 26.4 μs and 47.8 μs by using the XY4 and XY8 sequences, respectively.

The sensitivity of a spin-based magnetometer is limited by the photon shot noise when the readout is performed optically. An effective way to enhance the shot-noise limited sensitivity is to use a large number of NV spins which can enhance the collected PL signal significantly. Moreover, reduced dephasing and an enhancement in the coherence time of the NV spins can directly improve the sensitivity. Here, we try to overcome these issues by creating ensembles of

NV centers with superior coherence properties and examine the sensitivity of our possible NV-based magnetometer. Thus, following the speculation of Ref. [17], we can conclude that in ideal measurement conditions for an NV-based magnetometer exploiting the NV centers we prepared an NV concentration $\aleph = 22$ ppm and coherence time $T_2^* = 3.6$ μs can give a dc magnetic field sensitivity η_{dc} up to ~100 nT Hz$^{-1/2}$. On the other hand, by applying the DD sequences we could enhance the coherence time $T_2(\text{DD})$ significantly which can increase the sensitivity η_{ac} to ac magnetic field by a factor of $\sqrt{T_2(\text{DD})/T_2^*}$. For instance, using the DD sequence CPMG(64) we can obtain $\eta_{ac} \sim 10$ nT Hz$^{-1/2}$.

VI. CONCLUSION

Through this project we have described the deterministic preparation of ensembles of NV centers in ultrapure diamond films through three major steps: growing the diamond films, implanting the NV centers, and characterizing them. A plasma assisted CVD reactor for depositing high-purity diamond films was constructed and optimized to minimize the nitrogen content in the synthesized films. High-purity films with a thickness of 260 μm at a growth rate of about 30 μm/h with constant high crystal quality were deposited. The nitrogen content of the deposited diamond layers is below the detection limits of the standard methods of analytical chemistry or physics. The upper limit for nitrogen in our films was measured to be 1.3×10^{-7}(ca. 0.1 ppm) which refers to the fact that our films are at least among the purest diamond substrates that are commercially available. In the future we plan to perform measurements like EPR to see whether these samples are having even better purity than the commercially available ones.

An experimental setup for *in situ* preparation of the diamond surface, implantation, and high-temperature annealing has been presented. In conclusion it was observed that it is possible with this method to create NV centers while heating the diamond in UHV without strong defocusing effects. It was shown that it is possible to create localized NV centers on hydrogen-terminated and heated diamonds. Optimized implantation parameters have been obtained which enabled us to precisely implant NV centers. Using the above described implantation through an aperture, we could implant spots with sizes similar to the aperture of the ion gun in a deterministic way, thus achieving a better localization of the NV centers. The experimental protocol of large area scanning has been demonstrated which enables us to record the PL image of the full sample in millimeter scale with nanometer resolution. Optical spectroscopic measurements have ascertained the generation of NV centers. Next, we have demonstrated the potentiality for possible application of the created NV centers in quantum information and sensing by preserving the coherence for extended times. We observed that the NV spins respond well to different robust dynamical decoupling sequences. The coherence time T_2 has been extended and dephasing of the spins has been delayed in a controlled fashion. We can conclude that a magnetic sensor designed using the sample we prepared can reach a sensitivity of ~ 10 nT Hz$^{-1/2}$ under optimized experimental conditions.

In the future we plan to improve the coherence properties of the spins by creating NV centers in isotopically purified ^{12}C enriched diamond with ^{13}C concentration below 0.01% and improve the sensitivity to ac and dc magnetic field. Moreover, we plan to design an ion gun with nanometer aperture and install a single ion counter which will allow us to optimize the implantation dose and hence, the NV concentration. These experimental upgrades will allow us to deterministically implant ordered arrays of single NV centers which can function as an efficient large-scale solid-state quantum register.

[1] F. Jelezko and J. Wrachtrup, Phys. Stat. Sol. (a) **13**, 3207 (2006).

[2] F. Jelezko, T. Gaebel, I. Popa, M. Domhan, A. Gruber, and J. Wrachtrup, Phys. Rev. Lett. **93**, 130501 (2004).

[3] M. V. G. Dutt, L. Childress, L. Jiang, E. Togan, J. Maze, F. Jelezko, A. S. Zibrov, P. R. Hemmer, and M. D. Lukin, Phys. Rev. Lett. **316**, 1312 (2007).

[4] T. Chakraborty, J. Zhang, and D. Suter, New J. Phys. **19**, 073030 (2017).

[5] P. C. Maurer, G. Kucsko, C. Latta, L. Jiang, N. Y. Yao, S. D. Bennett, F. Pastawski, D. Hunger, N. Chisholm, M. Markham, D. J. Twitchen, J. I. Cirac, and M. D. Lukin, Science **336**, 1283 (2012).

[6] L. Childress *et al.*, Science **314**, 281 (2006).

[7] E. Togan, Y. Chu, A. S. Trifonov, L. Jiang, J. Maze, L. Childress, M. V. G. Dutt, A. S. Sørensen, P. R. Hemmer, A. S. Zibrov, and M. D. Lukin, Nature (London) **466**, 730 (2010).

[8] A. Sipahigil, M. L. Goldman, E. Togan, Y. Chu, M. Markham, D. J. Twitchen, A. S. Zibrov, A. Kubanek, and M. D. Lukin, Phys. Rev. Lett. **108**, 143601 (2012).

[9] H. Bernien, L. Childress, L. Robledo, M. Markham, D. Twitchen, and R. Hanson, Phys. Rev. Lett. **108**, 043604 (2012).

[10] G. D. Fuchs, G. Burkard, P. V. Klimov, and D. D. Awschalom, Nature Phys. **7**, 789 (2011).

[11] L. Childress, J. M. Taylor, A. S. Sørensen, and M. D. Lukin, Phys. Rev. Lett. **96**, 070504 (2006).

[12] L. M. Pham, D. L. Sage, P. L. Stanwix, T. K. Yeung, D. Glenn, A. Trifonov, P. Cappellaro, P. R. Hemmer, M. D. Lukin, H. Park, A. Yacoby, and R. L. Walsworth, New J. Phys. **13**, 045021 (2011).

[13] W. Liu, B. Naydenov, S. Chakrabortty, B. Wunsch, K. Hubner, S. Ritz, H. Colfen, H. Barth, K. Koynov, H. Qi *et al.*, Nano Lett. **16**, 6236 (2016).

[14] G. Balasubramanian, I. Y. Chan, R. Kolesov, M. Al-Hmoud, J. Tisler, C. Shin, C. Kim, A. Wojcik, P. R. Hemmer, A. Krueger, T. Hanke, A. Leitenstorfer, R. Bratschitsch, F. Jelezko, and J. Wrachtrup, Nature (London) **455**, 648 (2008).

[15] L.-S. Bouchard, V. M. Acosta, E. Bauch, and D. Budker, New J. Phys. **13**, 025017 (2011).

[16] J. Maze, P. Stanwix, J. Hodges, S. Hong, J. Taylor, P. Cappellaro, L. Jiang, M. G. Dutt, E. Togan, A. Zibrov *et al.*, Nature (London) **455**, 644 (2008).

[17] J. Taylor, P. Cappellaro, L. Childress, L. Jiang, D. Budker, P. Hemmer, A. Yacoby, R. Walsworth, and M. Lukin, Nat. Phys. **4**, 810 (2008).

[18] M. S. Grinolds, S. Hong, P. Maletinsky, L. Luan, M. D. Lukin, R. L. Walsworth, and A. Yacoby, Nat. Phys. **9**, 215 (2013).

[19] R. McDermott, S. K. Lee, B. t. Haken, A. H. Trabesinger, A. Pines, and J. Clarke, Proc. Natl. Acad. of Sci. USA **101**, 7857 (2004).

[20] D. Rugar, R. Budakian, H. Mamin, and B. Chui, Nature (London) **430**, 329 (2004).

[21] A. M. Chang, H. D. Hallen, L. Harriott, H. F. Hess, H. L. Kao, J. Kwo, R. E. Miller, R. Wolfe, J. van der Ziel, and T. Y. Chang, Appl. Phys. Lett. **61**, 1974 (1992).

[22] S. Xu, V. V. Yashchuk, M. H. Donaldson, S. M. Rochester, D. Budker, and A. Pines, Proc. Natl. Acad. of Sci. USA **103**, 12668 (2006).

[23] S. Hong, M. S. Grinolds, L. M. Pham, D. Le Sage, L. Luan, R. L. Walsworth, and A. Yacoby, MRS bulletin **38**, 155 (2013).

[24] V. M. Acosta, E. Bauch, M. P. Ledbetter, C. Santori, K.-M. C. Fu, P. E. Barclay, R. G. Beausoleil, H. Linget, J. F. Roch, F. Treussart, S. Chemerisov, W. Gawlik, and D. Budker, Phys. Rev. B **80**, 115202 (2009).

[25] A. U. C. Hardal, P. Xue, Y. Shikano, O. E. Müstecaplıoğlu, and B. C. Sanders, Phys. Rev. A **88**, 022303 (2013).

[26] X. Zhu, S. Saito, A. Kemp, K. Kakuyanagi, S.-i. Karimoto, H. Nakano, W. J. Munro, Y. Tokura, M. S. Everitt, K. Nemoto *et al.*, Nature (London) **478**, 221 (2011).

[27] X. Zhu, Y. Matsuzaki, R. Amsüss, K. Kakuyanagi, T. Shimo-Oka, N. Mizuochi, K. Nemoto, K. Semba, W. J. Munro, and S. Saito, Nat. Comm. **5**, 3524 (2014).

[28] S. Putz, D. O. Krimer, R. Amsuess, A. Valookaran, T. Noebauer, J. Schmiedmayer, S. Rotter, and J. Majer, Nature Phys. **10**, 720 (2014).

[29] W. L. Yang, Z.-q. Yin, Z. X. Chen, S.-P. Kou, M. Feng, and C. H. Oh, Phys. Rev. A **86**, 012307 (2012).

[30] B. Dischler, *CVD Diamond: A New and Promising Material* (Springer, Berlin, Heidelberg, 1998).

[31] F. Bundy, H. T. Hall, H. Strong, and R. Wentorf, Nature (London) **176**, 51 (1955).

[32] H. Liander, ASEA J. **28**, 97 (1955).

[33] B. Dischler and C. Wild, *Low-Pressure Synthetic Diamond: Manufacturing and Applications* (Springer Science & Business Media, 2013).

[34] G. Shu, B. Dai, V. Ralchenko, A. Khomich, E. Ashkinazi, A. Bolshakov, S. Bokova-Sirosh, K. Liu, J. Zhao, J. Han *et al.*, J. Cryst. Growth **463**, 19 (2017).

[35] H. Gnaser, Appl. Phys. Lett. **79**, 497 (2001).

[36] S. Jin and T. Moustakas, Appl. Phys. Lett. **65**, 403 (1994).

[37] G. Balasubramanian, P. Neumann, D. Twitchen, M. Markham, R. Kolesov, N. Mizuochi, J. Isoya, J. Achard, J. Beck, J. Tissler *et al.*, Nat. Mater. **8**, 383 (2009).

[38] J. Meijer, S. Pezzagna, T. Vogel, B. Burchard, H. Bukow, I. Rangelow, Y. Sarov, H. Wiggers, I. Plümel, F. Jelezko *et al.*, Appl. Phys. A **91**, 567 (2008).

[39] J. Meijer, B. Burchard, M. Domhan, C. Wittmann, T. Gaebel, I. Popa, F. Jelezko, and J. Wrachtrup, Appl. Phys. Lett. **87**, 261909 (2005).

[40] J. F. Ziegler, J. P. Biersack, and U. Littmark, *The Stopping Range of Ions in Matter* (SRIM, Co., Chester, MD, 2008).

[41] J. Rabeau, P. Reichart, G. Tamanyan, D. Jamieson, S. Prawer, F. Jelezko, T. Gaebel, I. Popa, M. Domhan, and J. Wrachtrup, Appl. Phys. Lett. **88**, 023113 (2006).

[42] S. Pezzagna, B. Naydenov, F. Jelezko, J. Wrachtrup, and J. Meijer, New J. Phys. **12**, 065017 (2010).

[43] S. Cui and E. L. Hu, Appl. Phys. Lett. **103**, 051603 (2013).

[44] B. Grotz, M. V. Hauf, M. Dankerl, B. Naydenov, S. Pezzagna, J. Meijer, F. Jelezko, J. Wrachtrup, M. Stutzmann, F. Reinhard *et al.*, Nat. Comm. **3**, 729 (2012).

[45] M. Kubovic, M. Kasu, H. Kageshima, and F. Maeda, Diam. Relat. Mater. **19**, 889 (2010).

[46] F. Maier, M. Riedel, B. Mantel, J. Ristein, and L. Ley, Phys. Rev. lett. **85**, 3472 (2000).

[47] F. Maier, J. Ristein, and L. Ley, Phys. Rev. B **64**, 165411 (2001).

[48] P. Siyushev, M. Nesladek, E. Bourgeois, M. Gulka, J. Hruby, T. Yamamoto, M. Trupke, T. Teraji, J. Isoya, and F. Jelezko, Science **363**, 728 (2019).

[49] A. M. Zaitsev, *Optical Properties of Diamond: A Data Handbook* (Springer Science & Business Media, Berlin/Heidelberg, 2013).

[50] M. W. Doherty, N. B. Manson, P. Delaney, F. Jelezko, J. Wrachtrup, and L. C. L. Hollenberg, Phys. Rep. **528**, 1 (2013).

[51] D. Suter and F. Jelezko, Prog. Nucl. Magn. Reson. Spectrosc. **98**, 50 (2017).

[52] L. M. Pham, Magnetic field sensing with nitrogen-vacancy color centers in diamond, Doctoral dissertation, Harvard University, Cambridge, Massachusetts, 2013.

[53] N. F. Ramsey, Phys. Rev. **78**, 695 (1950).

[54] E. L. Hahn, Phys. Rev. **80**, 580 (1950).

[55] N. Bar-Gill, L. Pham, C. Belthangady, D. Le Sage, P. Cappellaro, J. Maze, M. Lukin, A. Yacoby, and R. Walsworth, Nat. Comm. **3**, 858 (2012).

[56] L. M. Pham, N. Bar-Gill, C. Belthangady, D. Le Sage, P. Cappellaro, M. D. Lukin, A. Yacoby, and R. L. Walsworth, Phys. Rev. B **86**, 045214 (2012).

[57] T. D. Ladd, F. Jelezko, R. Laflamme, Y. Nakamura, C. Monroe, and J. L. OBrien, Nature (London) **464**, 45 (2010).

[58] G. De Lange, Z. Wang, D. Riste, V. Dobrovitski, and R. Hanson, Science **330**, 60 (2010).

[59] G. de Lange, D. Ristè, V. V. Dobrovitski, and R. Hanson, Phys. Rev. Lett. **106**, 080802 (2011).

[60] B. Naydenov, F. Dolde, L. T. Hall, C. Shin, H. Fedder, L. C. L. Hollenberg, F. Jelezko, and J. Wrachtrup, Phys. Rev. B **83**, 081201(R) (2011).

[61] C. A. Ryan, J. S. Hodges, and D. G. Cory, Phys. Rev. Lett. **105**, 200402 (2010).

[62] A. M. Souza, G. A. Álvarez, and D. Suter, Phil. Trans. R. Soc. A **370**, 4748 (2012).

[63] D. Suter and G. A. Álvarez, Rev. Mod. Phys. **88**, 041001 (2016).

[64] N. Bar-Gill, L. M. Pham, A. Jarmola, D. Budker, and R. L. Walsworth, Nat. Comm. **4**, 1743 (2013).

[65] A. A. Maudsley, J. Magn. Reson. **69**, 488 (1986).

[66] A. M. Souza, G. A. Álvarez, and D. Suter, Phys. Rev. Lett. **106**, 240501 (2011).